

Supplementary information

Cobalt hexacyanoferrate as a selective and high current density formate oxidation electrocatalyst

Lijuan Han,^a Jesús González-Cobos,^a Irene Sánchez-Molina,^a Stefano Giancola,^a Scott J. Folkman,^a Pengyi Tang,^b Marc Heggen,^c Rafal E. Dunin-Borkowski,^c Jordi Arbiol,^{b,d} S. Giménez^e and Jose Ramon Galan-Mascaros^{*,a,d}

^aInstitute of Chemical Research of Catalonia (ICIQ), The Barcelona Institute of Science and Technology (BIST), Av. Paisos Catalans, 16. Tarragona, E-43007, Spain.

^bCatalan Institute of Nanoscience and Nanotechnology (ICN2), CSIC and BIST, Campus UAB, Bellaterra, 08193 Barcelona, Catalonia, Spain.

^cErnst-Ruska Centre for Microscopy and Spectroscopy with Electrons and Peter Grünberg Institute, Forschungszentrum Jülich GmbH, 52425 Jülich, Germany.

^dICREA, Pg. Lluís Companys 23, 08010 Barcelona, Spain.

^eInstitute of Advanced Materials (INAM), Universitat Jaume I, 12006 Castelló, Spain.

Supplementary discussion: EIS analysis

We have initially considered a classical physical model, which has been successfully employed in nanoporous electrodes for water splitting (**Figure S13a**)¹⁻³. In this model, we consider that the FTO substrate (C_{FTO}) is in contact with the electrolyte, since FTO can transfer to the CoFePB (C_{CoFePB}) nanoporous layer, and additionally to the solution (R_{FTO}). Charge transport (r_t) and charge transfer to the solution (r_{ct}) are distributed and coupled along the electrode thickness and a transmission line element conveys this information, together with the capacitance of the CoFePB/solution interface (C_{CoFePB}). Charge transfer at the FTO/CoFePB interface is modeled by a parallel RC element ($R_{\text{FTO/CoFePB}}/C_{\text{FTO/CoFePB}}$) and the impedance of the solution is modeled by a Warburg element (Z_d), R_s is the series resistance, which conveys the resistance of the contact and wiring. Since we did not identify any 45 degrees line in any of the obtained Nyquist plots, we omitted the transmission line as a first simplification of this model (**Figure S13b**). We further simplified the model omitting the charge transfer from the FTO to the solution (**Figure S13c**), since this element should respond at higher frequencies than those employed in the current measurements ($>10^5$ Hz).

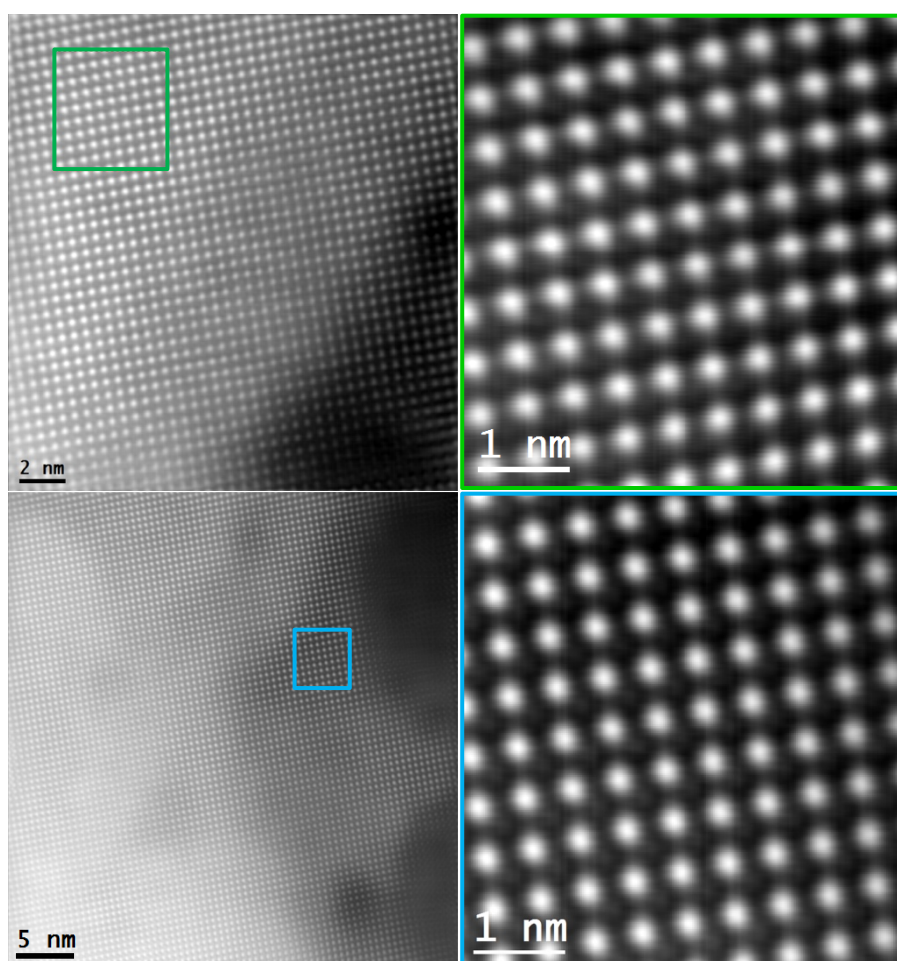


Figure S1. Left top: atomic resolution HAADF STEM general view images showing the crystal structure from the bulk region of the nanocubes, Right top: atomic scale magnified view showing the crystal structure from the bulk region of the nanocubes. Left bottom: atomic resolution HAADF STEM general view images showing the crystal structure from the edge region of the nanocubes, Right bottom: atomic scale magnified view showing the crystal structure from the edge region of the nanocubes.

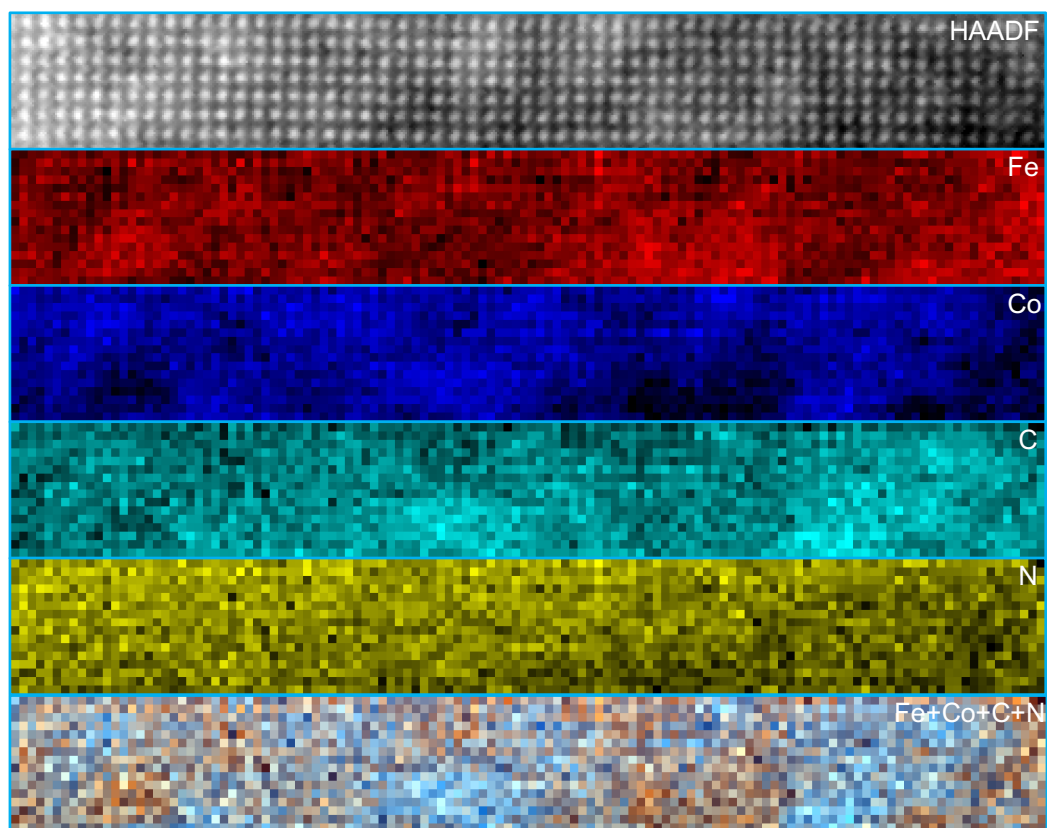


Figure S2. EELS chemical composition maps obtained on the HAADF-STEM selected view on top. Individual Fe (red), Co (blue), C (indigo), N (yellow) maps and their composite.

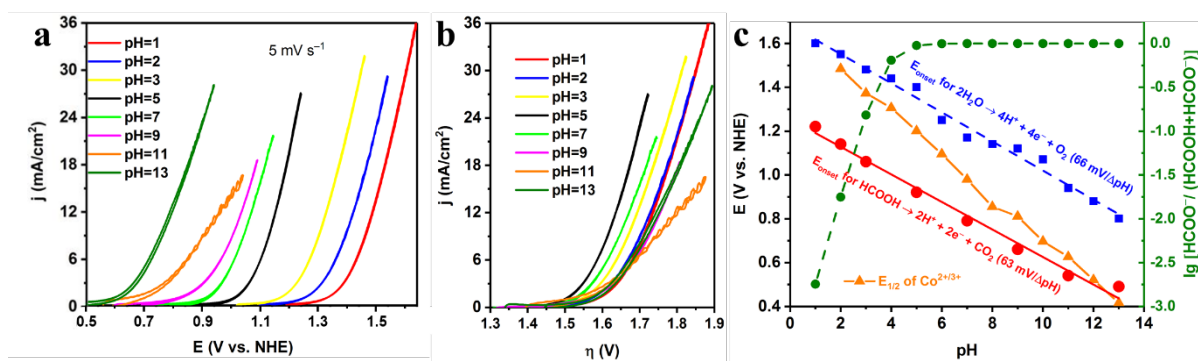


Figure S3. Cyclic voltammetry (5 mV s^{-1}) of a 0.4 M HCOO^- in 0.1 M phosphate electrolyte (KPi), which was prepared by dissolving K_2HPO_4 and KH_2PO_4 in 1 M KNO_3 solution as a function of pH with (a) the potential vs NHE and (b) the same data represented as overpotential vs the standard potential of formate oxidation. Both forward and backward scans are presented but are difficult to see due to the similarity in current for both the forward and reverse scans—indicating the steady-state nature of this experiment and lack of poisoning due to oxidation intermediates. Lastly, (c) representation of the estimated onset potential for the oxidation of $\text{HCOOH}/\text{HCOO}^-$ (red), and H_2O (blue) as well as the $\text{Co}^{\text{II}}/\text{Co}^{\text{III}}$ redox pair (orange) and the formate/formic acid speciation as a function of pH.

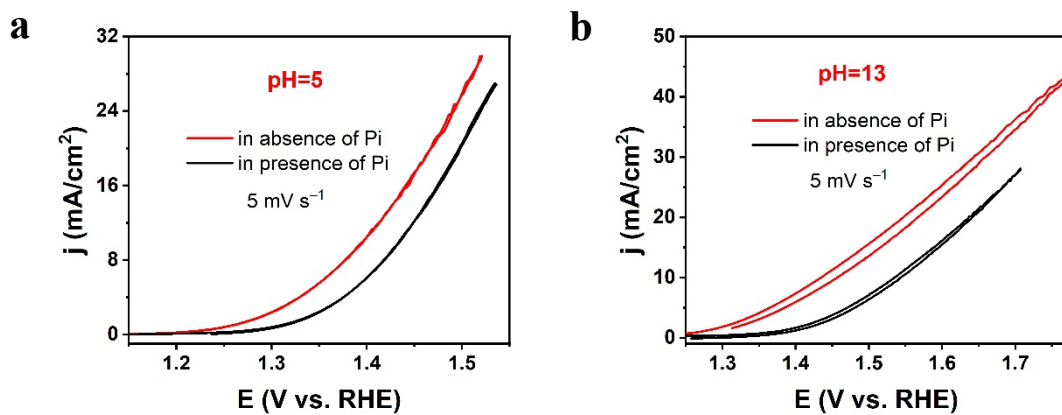


Figure S4. Cyclic Voltammograms with a CoFePB working electrode in 0.4 M formate aqueous solution containing (red curve) or not (black curve) phosphate anions at pH 5 (**a**) and pH 13 (**b**).

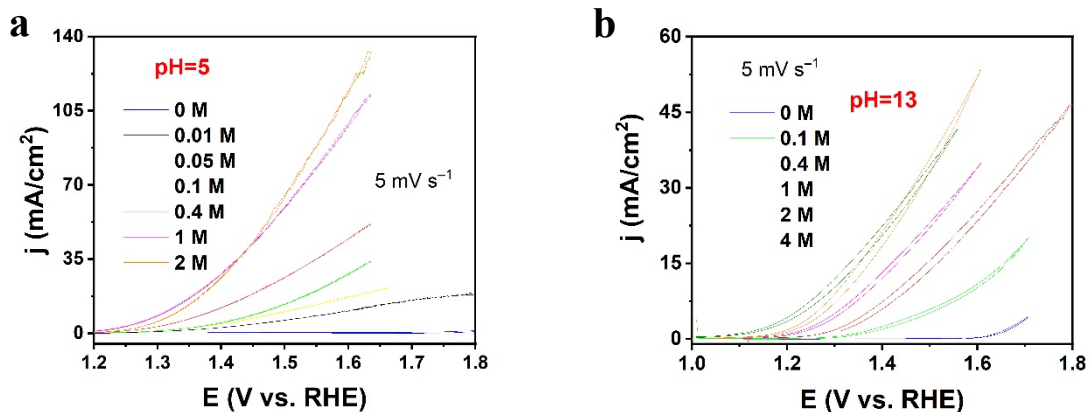


Figure S5. Cyclic voltammogram with a CoFePB working electrode in 1 M KNO₃ (in the absence of KPi) aqueous solution at a) pH 5 and b) pH 13, containing various formate concentrations with scan rate 5 mV s⁻¹.

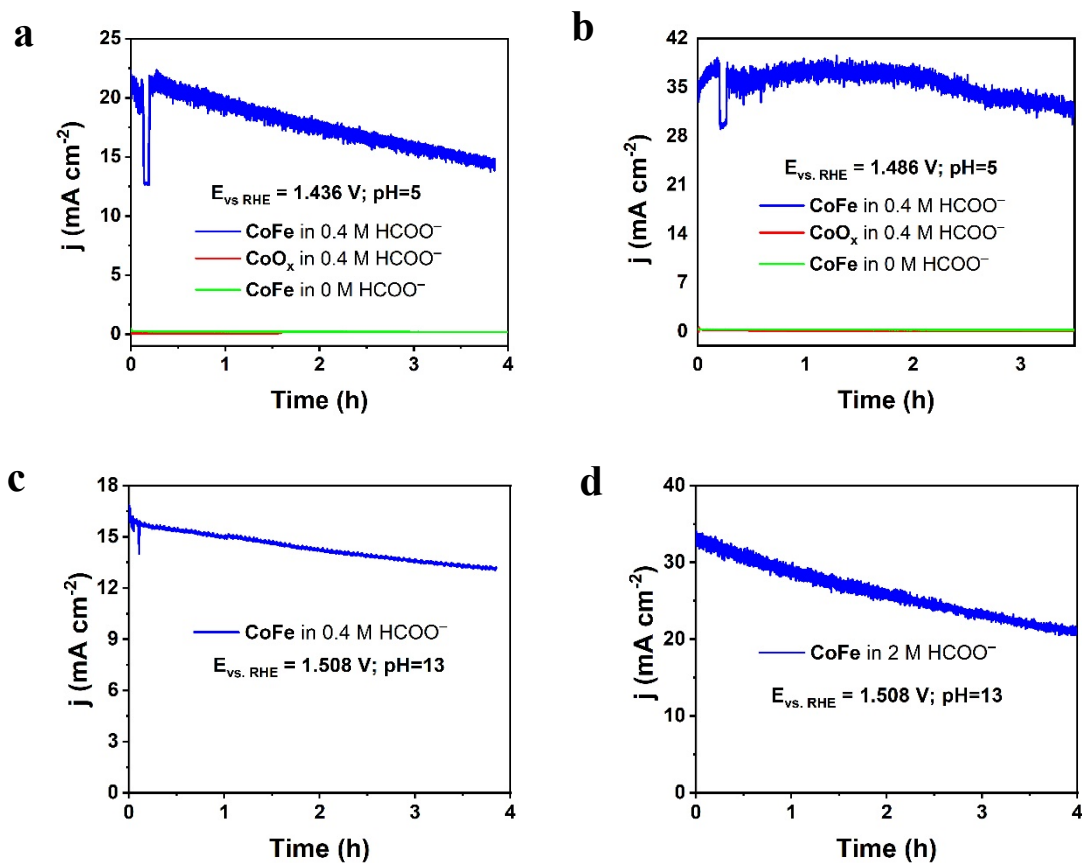


Figure S6. Chronoamperometry (CA) on CoFePB (a) at 1.436 V vs. RHE in 0.4 M HCOOH/HCOO⁻ aqueous solution at pH 5. (b) at 1.486 V vs. RHE in 0.4 M HCOOH/HCOO⁻ aqueous solution at pH 5. (c) at 1.508 V vs. RHE in 0.4 M HCOO⁻ aqueous solution at pH 13, (d) at 1.508 V vs. RHE in 2.0 M HCOO⁻ aqueous solution at pH 13.

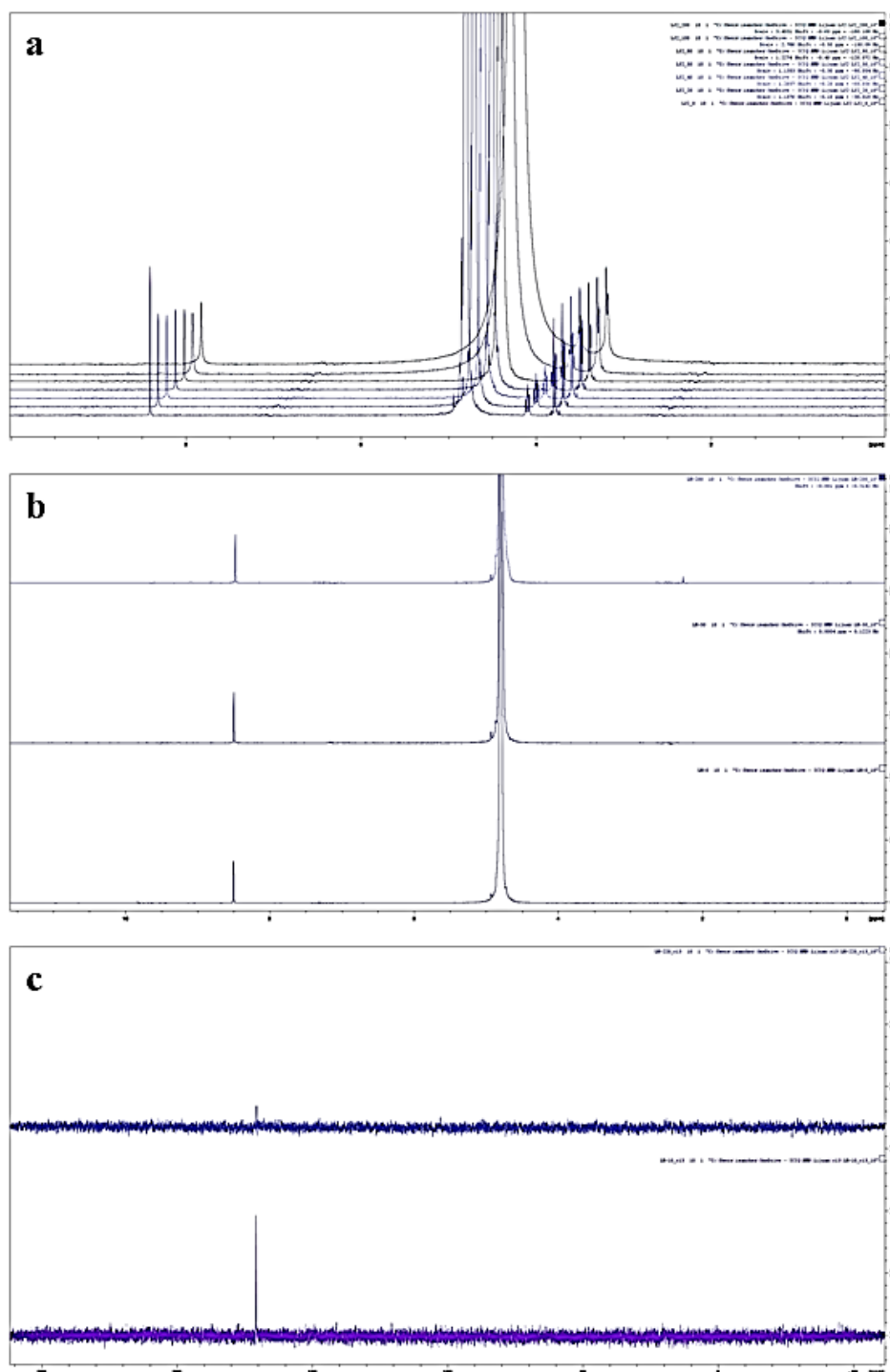


Figure S7. (a) Selected ^1H -NMR spectra of samples extracted at various time intervals (0, 20, 40, 50, 80, 100 and 200 min) during chronoamperometric measurement at 1.486 V vs. RHE in 1 M KNO_3 solution containing 0.4 M $\text{HCOOH}/\text{HCOO}^-$ (pH 5). Ascorbic acid was added as a reference, at a fixed concentration of 0.2 M, (b) ^1H ^{13}C NMR spectra in D_2O of samples taken during the catalytic experiments, (c) ^{13}C NMR. The only signal observed is the one belonging to formic/formate, at 8.41 ppm in ^1H -NMR and 171 ppm in ^{13}C -NMR. We do not observe in ^1H -NMR products such as formaldehyde or methanol that would arise from reduction reactions.

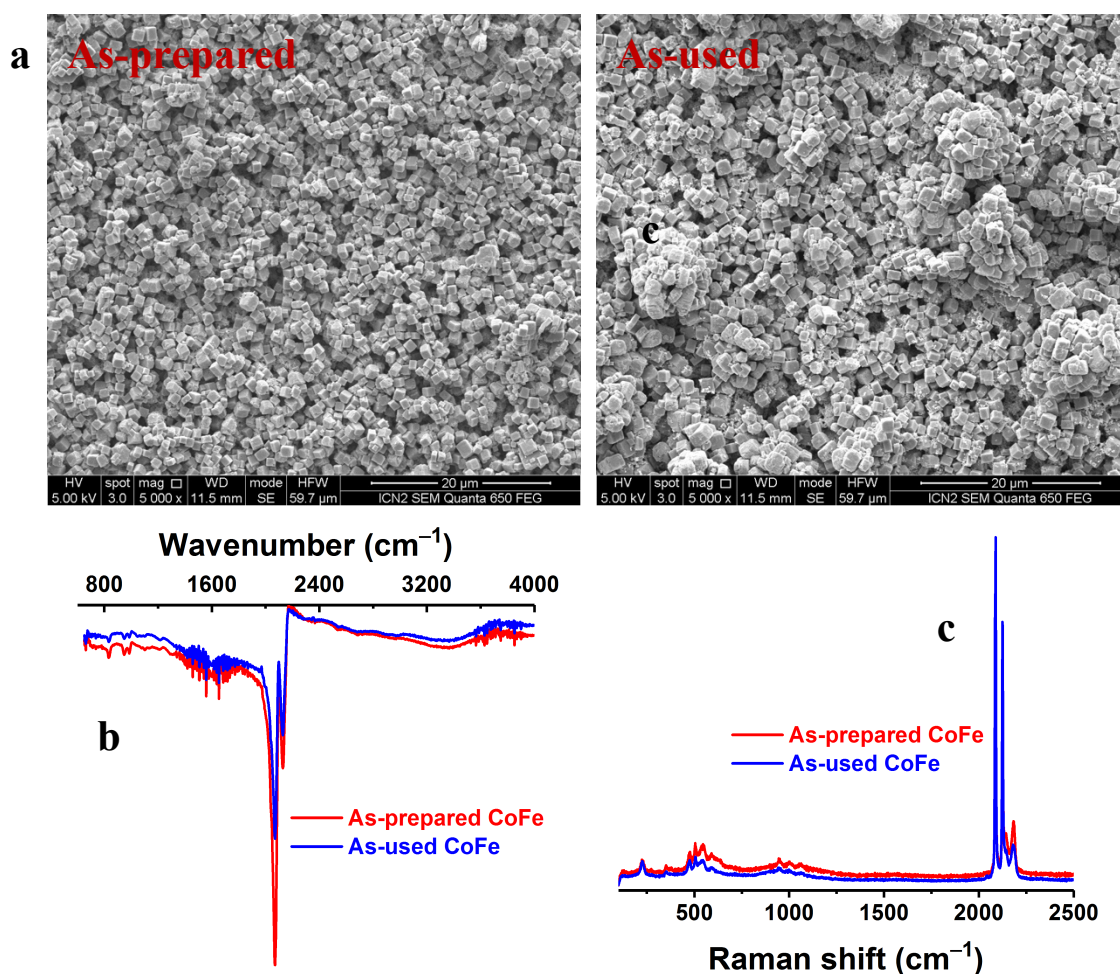


Figure S8. Characterization of CoFePB electrodes after a 4h chronoamperometry in 0.4 M HCOOH/HCOO⁻ aqueous pH 13 solution. (a) SEM image. (b) Raman spectra. (c) Infrared spectra.

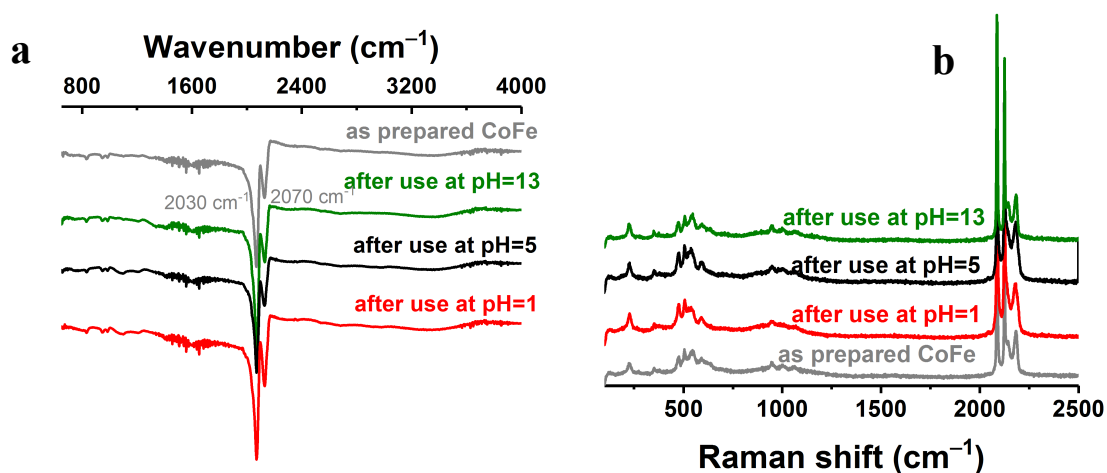


Figure S9. Characterization of CoFePb electrodes after chronoamperometry in 0.4 M HCOOH/HCOO⁻ aqueous solution at different pH. (a) Infrared spectra. (b) Raman spectra.

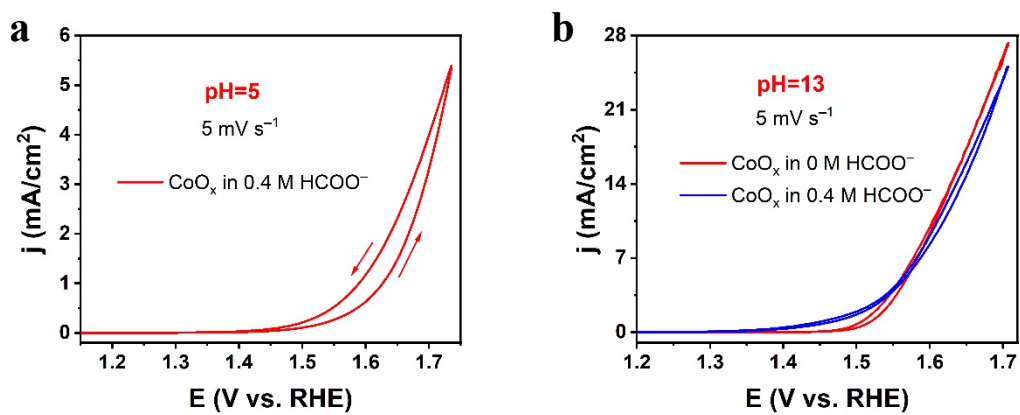


Figure S10. CVs at 5 mV s⁻¹ on CoO_x working electrodes in 0.4 M HCOOH/HCOO⁻ aqueous solution at pH 5 (a) and pH 13 (b).

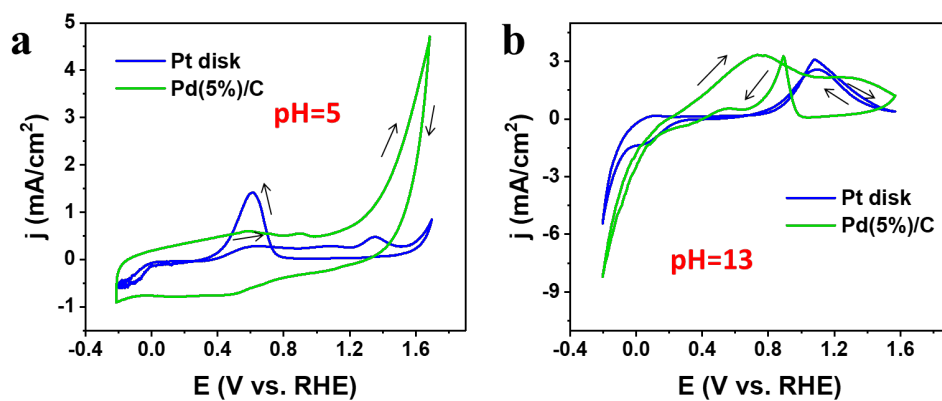


Figure S11. CVs at 5 mV s^{-1} on Pt disk and Pd(5%)/C electrodes in $0.4 \text{ M HCOOH/HCOO}^-$ aqueous solution at pH 5 (a) and pH 13 (b).

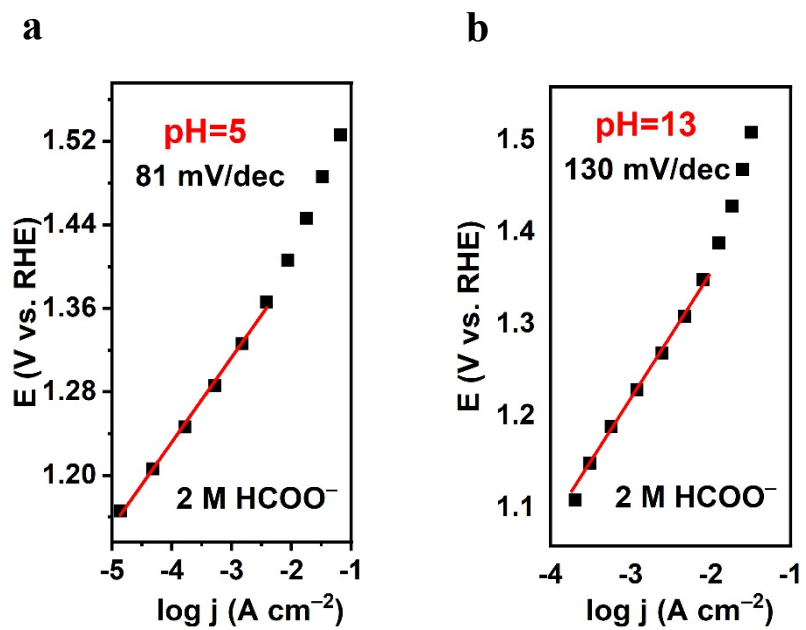


Figure S12. Tafel plots from steady-state chronoamperometric data obtained with CoFePB electrodes in 2 M HCOOH/HCOO^- aqueous solution at pH 5 (a) and pH 13 (b).

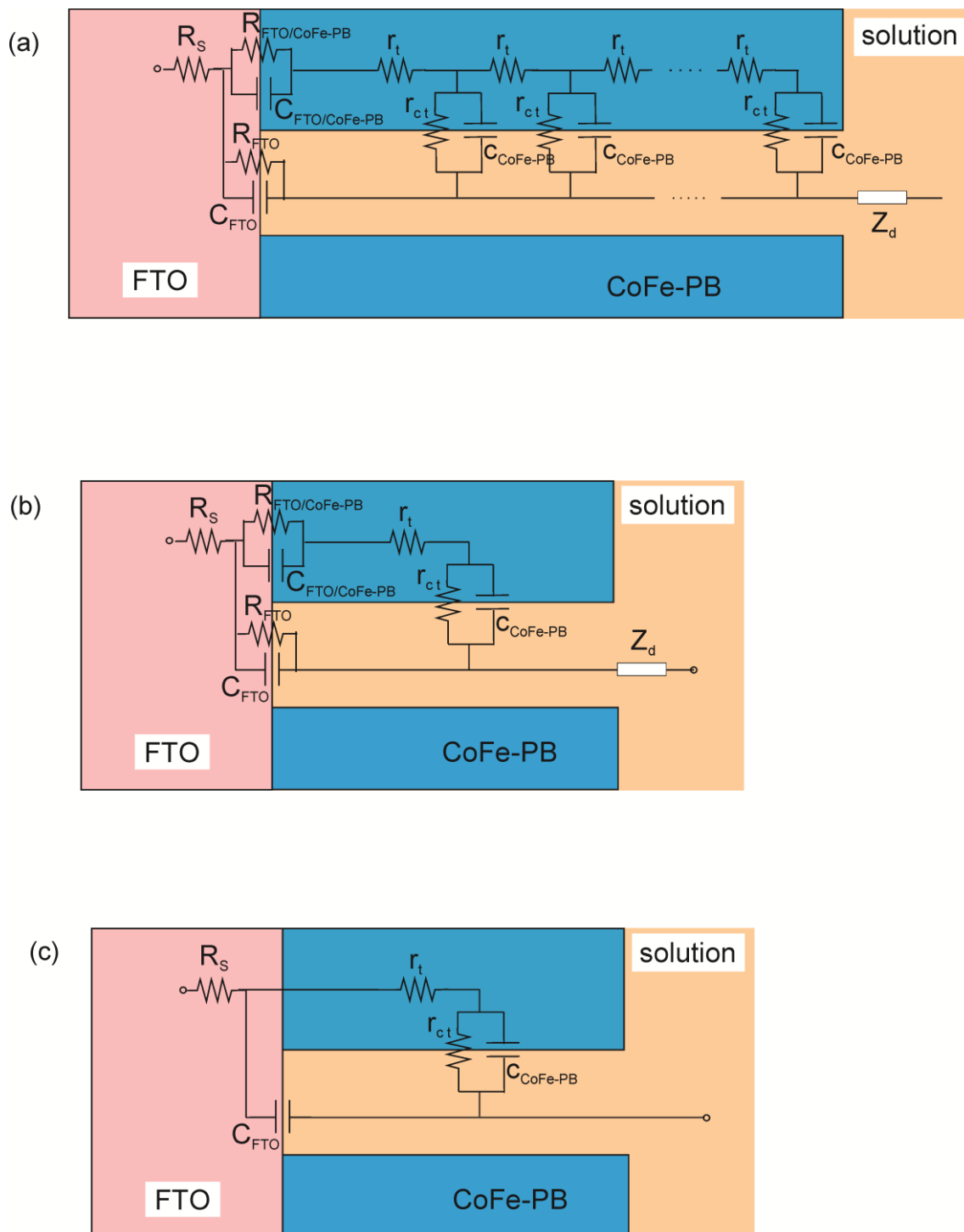


Figure S13. (a) Equivalent circuit employed for nanostructured FTO/CoFePB electrodes in contact with a liquid solution. (b) Simplified circuit without the transmission line element. (c) Final circuit employed to fit the raw impedance data, where charge transfer to the solution from FTO is not allowed and without the impedance at the solid-state FTO/CoFePB interface, which should respond at frequencies higher than 10^5 Hz.

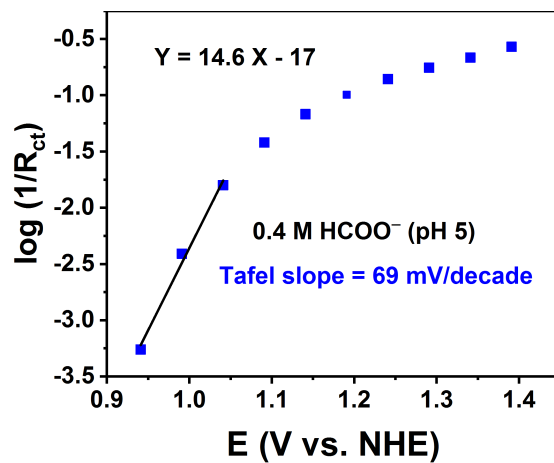


Figure S14. Dependence of R_{ct} for $\text{HCOOH}/\text{HCOO}^-$ electro-oxidation on electrode potentials at pH 5.

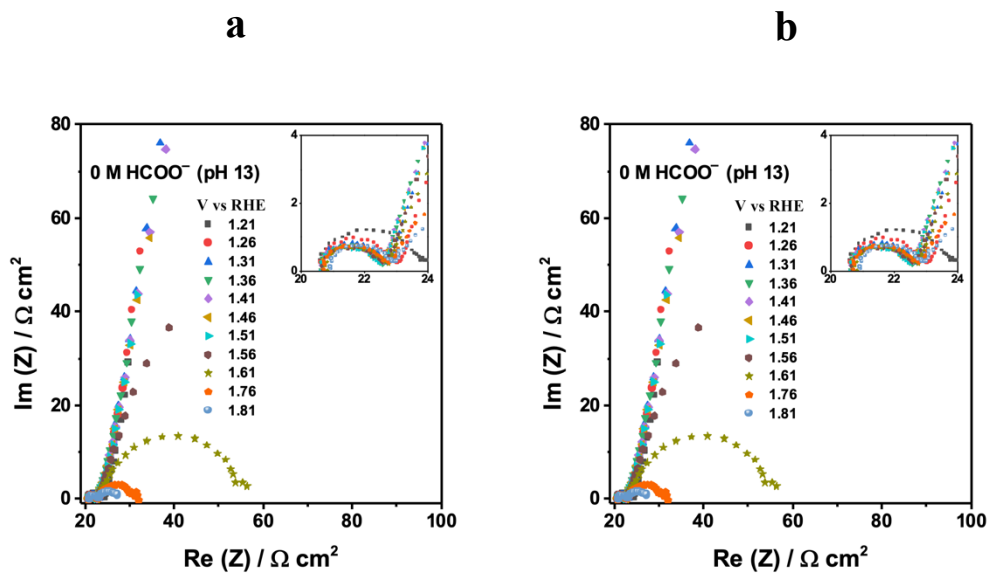


Figure S15. Complex-plane impedance plots of CoFe electrode in 1 M KNO_3 solution in the absence of $\text{HCOOH}/\text{HCOO}^-$ at pH 5 (a) and pH 13 (b) measured at various polarization potentials given in the figure legends. The insert shows the high-frequency portion of the data in enlarged fashion.

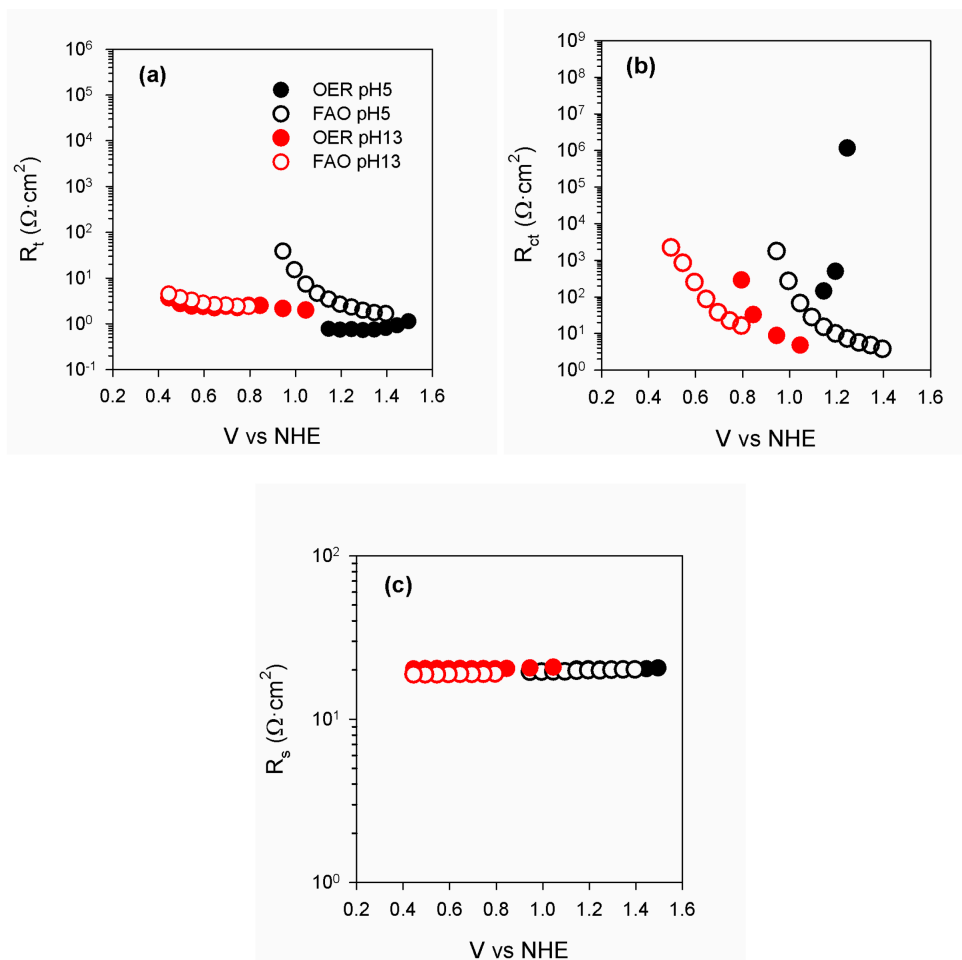


Figure S16. EIS data for CoFePB electrodes in the presence (open circles) or absence (full circles) of $\text{HCOOH}/\text{HCOO}^-$ comparing formic acid oxidation (FAO) vs oxygen evolution reaction (OER) at pH 5 (black color) and pH 13 (red color). (a) Transport resistances (R_t). (b) Charge transfer resistances (R_{ct}). (c) Series resistance (R_s).

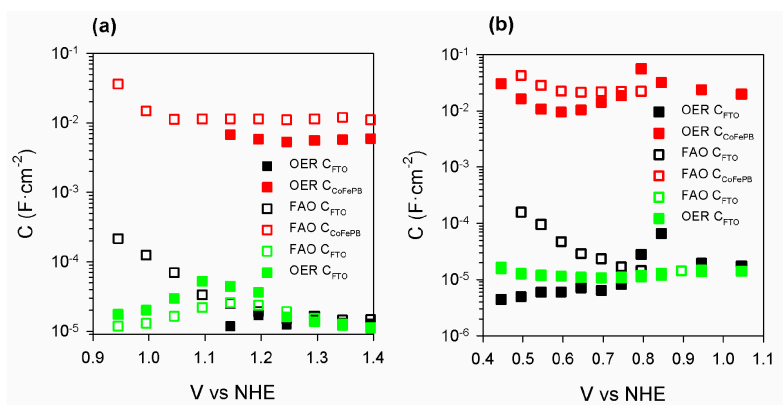


Figure S17. Extracted capacitances from the model in **Figure S15** in the presence (FAO, empty symbols) or absence (OER, full symbols) of $\text{HCOOH}/\text{HCOO}^-$ at pH 5 **(a)** or pH 13 **(b)**. The capacitances for the FTO/solution interface (C_{FTO} , black color) and for the CoFePB/solution (C_{CoFePB} , red color) are showed. The capacitances from blank measurements on bare FTO substrates are also included in green color to validate the obtained results.

Table S1. CO₂ faradaic efficiencies calculated from the steady-state MS signals obtained for m/z ratios of 44 and 22 at different applied current densities, at pH 5, 1 M KNO₃ and 0.4 M Formate.

Current density / mA cm ⁻²		5	10	15
Theoretical CO ₂ flow / NmL min ⁻¹		0.037	0.075	0.112
m/z=44	Steady ion current / A	4.30e-10	8.87e-10	1.26e-9
	CO ₂ concentration in outlet stream / %	0.068	0.015	0.217
	CO ₂ flow / NmL min ⁻¹	0.034	0.075	0.109
	CO₂ faradaic efficiency / %	90.5	100.4	97.0
m/z=22	Steady ion current / A	5.12e-12	9.11e-12	1.32e-11
	CO ₂ concentration in outlet stream / %	0.080	0.157	0.236
	CO ₂ flow / NmL min ⁻¹	0.040	0.079	0.118
	CO₂ faradaic efficiency / %	107.8	105.5	105.7

Table S2. Relative intensities obtained between the signals of carbon dioxide molecular ion and some of its fragment ions under the conditions shown in Table S1.

Ion	m/z	NIST Standard Relative intensity / % ⁴	5 mA cm ⁻²		10 mA cm ⁻²		15 mA cm ⁻²	
			Steady ion current / A	Relative intensity / %	Steady ion current / A	Relative intensity / %	Steady ion current / A	Relative intensity / %
CO ₂ ⁺	44	100	4.30E-10	100	8.87E-10	100	1.26E-09	100
C ⁺	12	8.7	3.87E-11	9.0	7.23E-11	8.2	1.02E-10	8.1
CO ₂ ⁺⁺	22	1.9	5.12E-12	1.2	9.11E-12	1.0	1.32E-11	1.0
C ¹⁸ O-O ⁺	46	0.4	2.08E-12	0.5	3.95E-12	0.4	5.27E-12	0.4

Reference

- (1) Mora-Sero, I.; Gimenez, S.; Fabregat-Santiago, F.; Gomez, R.; Shen, Q.; Toyoda, T.; Bisquert, J. *Acc. Chem. Res.* **2009**, *42*, 1848.
- (2) Gimenez, S.; Dunn, H. K.; Rodenas, P.; Fabregat-Santiago, F.; Miralles, S. G.; Barea, E. M.; Trevisan, R.; Guerrero, A.; Bisquert, J. *J. Electroanal. Chem.* **2012**, *668*, 119.
- (3) Fabregat-Santiago, F.; Bisquert, J.; Garcia-Belmonte, G.; Boschloo, G.; Hagfeldt, A. *Sol. Energy Mater. Sol. Cells* **2005**, *87*, 117.
- (4) Carbon dioxide. National Institute of Standards and Technology (NIST). U.S. Department of Commerce, <https://webbook.nist.gov/cgi/cbook.cgi?ID=C124389&Mask=200#Mass-Spec> (Accessed December 16, 2019).